Carbon dioxide as a line active agent: its impact on line tension and nucleation rate

Romain Bey, Benoit Coasne, Cyril Picard

Carbon dioxide as a line active agent: its impact on line tension and nucleation rate

Romain Bey[a], **Benoit Coasne**[a,1], **and Cyril Picard**[a,1]

[a]Univ. Grenoble Alpes, CNRS, LIPhy, 38000 Grenoble, France

This manuscript was compiled on September 2, 2021

By considering a water capillary bridge confined between two flat walls, we investigate the thermodynamics of the triple lines delimiting this solid-liquid-vapor system when supplemented in carbon dioxide. By means of atom-scale simulations, we show that carbon dioxide accumulates at the solid walls and, preferably, at the triple lines where it plays the role of a line active agent. The line tension of the triple lines, which is measured with an original mechanical approach, is shown to be driven by the line excess concentrations of the solute (carbon dioxide) and solvent (water). Solute accumulation at the lines tends to decrease the negative line tension (i.e. more negative) while solvent depletion from the lines has the opposite effect. Upon increasing the carbon dioxide partial pressure, the absolute value of the negative line tension increases – by more than an order of magnitude in the presence of hydrophilic walls when the carbon dioxide pressure exceeds 3 MPa. We finally show that the coupling between line and surface effects induced by gaseous adsorption leads to a non trivial impact on heterogeneous nucleation when considering nanometric critical nucleus.

Adsorption | siliceous zeolites | phase diagram | separation | catalysis

Line tension, a concept introduced by Gibbs in the late nineteenth century, is still mostly considered as an academic curiosity. In the spirit of excess quantities used to characterize an interface, such as surface tension, Gibbs suggested that lines separating several interfaces may also be endowed with excess quantities. In particular, the excess free energy per unit length of such a line is called the line tension. It can be seen as a force with the underlying image of the tension in a thread whose diameter is of a molecular size. It has been considered for a long time that the contribution of such a force is limited to the molecular or maybe to the nanometer scale. Line tension for instance plays a key role in the first-order transition leading to phase separation within a lipid layer. The nucleation of rafts within a biological membrane is a archetypical example illustrating such a thermodynamical contribution; the nucleation of such a two-dimensional phase within the lipid layer generates lines whose tension is generally lower than the pN (1, 2). Some studies even suggest that line tension may be lowered by line active agents – the so-called lineactants – namely surfactants which present a specific affinity for the line in addition to their affinity for the interface (3). As shown in this paper, the concept of lineactant is not restricted to the sole bi-dimensional space in interfaces. Rowlinson and Widom already envisioned theoretically in 1982 the possibility of adsorption at a triple line separating three-dimensional phases and its subsequent impact on line tension(4).

As demonstrated by Gretz in 1966, the line tension may be directly involved in heterogeneous nucleation. This process is indeed characterized by the presence of a triple line between the nucleus and the preexisting phases (5). This result is essential as it makes a bridge between the nanoscale contribution of the triple line and macroscopic events subsequent to nucleation. For instance, it has been shown theoretically that the line tension may contribute to water condensation on atmospheric aerosols and cloud formation (6). These various atmospheric aerosols can originate from multicomponent nucleation of trace condensable vapors – in particular water, acids, bases and organics (7, 8). If the line tension has to be considered in this field, several chemical species may contribute to its value. The determination of the line tension, however, is still a matter of debate even for a triple line involving the vapor and liquid phases for a single fluid on a well-defined solid surface. From a thermodynamical viewpoint, the line tension can be positive or negative while preserving the coexistence of the adjacent phases (4). Nevertheless, in the particular case of solid/liquid/vapor triple lines, recent works indicate that a negative sign is mainly expected apart for a system close from the wetting transition (9, 10). For instance, for ordered hydrophobic nanopores of a few nm in diameter, it has been shown experimentally and confirmed numerically that large drying pressures of more than 200 bars are induced by a negative line tension. In fact, such a negative line tension favors the emergence of a gas nucleus at the origin of the drying process (11, 12). Without such a negative line tension, the energy barrier associated to the nucleation process would be significantly larger so that the system would remain stable and

Significance Statement

The formation of any three-phase system at the nanoscale, through heterogeneous nucleation, may be controlled by the free energy cost of the triple line, characterized by its line tension. The precise contribution of line tension is still fuzzy due to a lack of robust quantitative values, although a consensus start to emerge concerning the case of solid/liquid/vapor system with a pure fluid. Line tension effects might matter in numerous fields, such as process and chemical engineering (phase transitions, electrochemistry), but also biology (evagination of nano-vesicle) or geophysics (cloud formation from aerosol, fluid sequestration in porous media). In these different fields fluids are rarely pure. While surface effects are known to be strongly dependent on adsorption of solute, the case of triple line remains to be explored. Our results show that CO_2 acts as a line active agent which can significantly alter the value of line tension, reinforce its effect and strongly impact heterogeneous nucleation.

Please provide details of author contributions here.

The authors declare no conflict of interest.

[1]To whom correspondence should be addressed. E-mail: benoit.coasne univ-grenoble-alpes.fr, cyril.picard univ-grenoble-alpes.fr,

saturated in water at atmospheric pressures. This example shows that the line tension, which balances with surface and bulk thermodynamical contributions, acts as a lever controlling the state and stability of fluids in confinement (13). Industrial and geophysical processes related to boiling and condensation but also gas production and storage in nanoporous media are directly concerned (14).

The thermodynamic state and stability of a mixture of water and non-condensable soluble gases as well as the kinetics of phase transition in such a mixture remain a recurrent issue. Among numerous examples, this aspect is well illustrated in the framework of climate change mitigation and associated energy transition. These questions are central for instance to the modeling of CO_2 geological capture in aquifers (18–21). This issue is also pregnant in the formation and stability of gas clathrates – in particular, methane hydrate trapped in seafloor and rocks as they correspond to critical amounts of greenhouse gases potentially harmful to the environment (22–24). Meanwhile, such clathrates are also regarded as a promising way to store temporarily renewable energy with the development of power to gas strategies. In this context, hydrogen plays also a central role, either combined with CO_2 to generate methane or used directly as an energy vector. Major efforts aim at the improvement of the efficiency of water electrolysis, as a green way to produce hydrogen, and electricity production based on hydrogen fuel cell. The core of both devices is based on a confined reactive zone which leads to the nucleation of either gas bubbles within water in electrolyzers or water droplets within gas in fuel cells (25, 26). An additional issue to be addressed concerns the storage of hydrogen envisioned for instance in hydrophilic nanoporous materials (27). Up to now, when addressing these specific topics and, more generally, the question of the state of confined water/gas mixture (either for technological problems or biological processes (28)), the role of line tension has been often overlooked (29). The contribution of contact lines in heterogeneous nucleation with respect to volume and surface free energy contributions is directly related to the value of the line tension which has remained for long a barely known quantity. For model systems, a consensus starts to emerge concerning the line tension related to a solid/liquid/vapor triple line for a single fluid. For water, these values are generally negative and of the order of a few pN (9, 11, 12, 29–33). However, the case of a fluid mixture with potential accumulation of one species at the triple line is still an open problem, which is also of prime interest for the physics of oversolubility aspects which refer to the large gas solubility increase in liquids confined in nanoporous solids with respect to the value predicted from Henry's law (15–17).

While a few experiments suggest that dissolved gas may accumulate at solid interfaces and influence nucleation acting as surfactants (34–38), there is no quantitative data concerning their contribution to a triple line. Does a gas solute behave as a line active agent at a triple line? Would such solute excess at the line impact heterogeneous nucleation rates?

We address these questions using molecular dynamics simulations for an infinite liquid droplet confined between two flat solid walls – hence forming four straight triple lines which are the locus of specific molecular structuring (see Fig. 1). The droplet, which is invariant by translation in the y direction, is modeled by a finite system confined in a rectangular box to which periodic boundary conditions are applied in the three directions of space. The system is made of water molecules in the liquid state (solvent) and of CO_2 molecules (solute) in the gas state and partly solubilized in water. This fluid mixture is at constant temperature T and constant numbers of solvent and solute molecules. Molecular simulations are performed using LAMMPS software (39) with a Verlet integration algorithm coupled to a Nosé-Hoover thermostat. The two curved liquid-gas interfaces intersect the solid walls along the triple lines with a contact angle θ_Y. The distance h between the walls is such that disjoining pressure effects are negligible (see Supplementary Information) . As the triple line is straight, its tension does not contribute to the contact angle (9) so that θ_Y corresponds to Young's contact angle. This paper is focused on water/CO_2 mixtures – a key system of interest for applied and basic sciences – in contact with either hydrophilic or hydrophobic walls. We aim at addressing the question of adsorption at the triple line which is coupled to adsorption at surfaces. We do not consider any chemical reaction such as the formation of a small amount of carbonic acid from the dissolution of CO_2 in water (which is known to occur in real systems).

The thermodynamical properties of the system – in particular, the line tension and line excess concentrations – are studied as a function of the solute partial pressure in the gas phase. To determine the line tension of the straight solid/liquid/gas triple lines, we use a recently introduced mechanical methodology which offers unprecedented sensitivity and reliability(9). The line tension is directly extracted from force measurements. More precisely, as detailed in the Materials and Methods section, the specific contribution of the line in the y direction is separated from the bulk and surface contributions determined using force measurements in the x and z directions as the line tension is not acting in these directions (9) (Fig. 1). The line excess concentrations are readily obtained by subtracting bulk and surface excess quantities to the total amount of fluid molecules for each species. The measurement approach is further detailed in the Materials and Methods section.

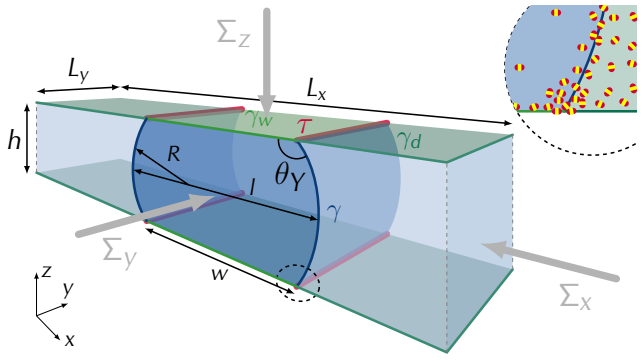

Fig. 1. Set-up consisting of a liquid (dark blue) in contact with a partially soluble gas confined between two solid walls (perpendicular to the z direction). Solid/fluid and liquid-gas interfaces are separated by distances h and l, respectively. The dependence of the line tension τ on the adsorption of molecules at the straight contact lines (in red, see zoom) is estimated from the forces Σ_x, Σ_y and Σ_z exerted along x, y and z.

Water/carbon dioxide confined mixtures

We consider the case of water/CO_2 mixtures in nanoconfinement – which is a system of particular relevant to geological sequestration of greenhouse gases. Fig. 2A shows the CO_2 density map for a liquid water droplet in contact with gaseous CO_2 (partial pressure $p_g = 4.3$ MPa) and confined between two hydrophobic walls. CO_2 molecules present an affinity for the interfaces, especially for the triple line. The local CO_2 concentration is indeed larger at interfaces compared to bulk phases and even twice larger in the vicinity of the triple line than at any other point close to the solid/gas interface (Fig. 2B). Adopting Gibbs modeling (4), these larger densities can be accounted for by using excess quantities defined as molecules per unit area (surface adsorption) or per unit line (linear adsorption). Once the geometric location of the different surfaces are defined using the solvent zero-adsorption criterion, the position of the triple line is readily obtained from the intersection of the wall position and that of the liquid/gas interface (without any additional criterion on the line excess concentration). As a consequence of such positioning convention, both the solute and solvent line excess concentrations may be non-zero so that they contribute to the thermodynamics of the triple line. Fig. 3B presents the water and CO_2 line concentrations as a function of the CO_2 partial pressure p_g. The CO_2 line concentration increases with p_g while the water line concentration diminishes. This corresponds to the replacement of solvent molecules by solute molecules at the triple line. It is worth noting that the triple line appears, in both hydrophilic and hydrophobic cases, as a water depleted region for all CO_2 pressures. CO_2 accumulates in the first molecular layer at the solid surface while water depletion occurs on 2 to 3 molecular layers (see Supplementary Information). Such water depletion and CO_2 accumulation at the line is more pronounced for the hydrophilic solid than the hydrophobic solid (see Fig. 3B). This somewhat counter-intuitive result can be rationalized by considering oversolubility effects which are known to occur in nanoconfined solvents (17). In particular, it was shown that such oversolubility pertains either to direct surface adsorption or to solvent molecular structuration at the vicinity of the surface (15). In the first case, oversolubility is due to the preferential adsorption of the solute directly in contact with the surface. In the second case, oversolubility is due to increased solubility of the solute in the density minima appearing with the strong layering of the solvent at the surface. Here, considering that CO_2 adsorption is more marked in the hydrophilic case, our results suggest that CO_2 increased adsorption at the solid-liquid interface pertains to an oversolubility induced by the strong layering of water at the surface (indeed, more pronounced layering is expected for hydrophilic surfaces than hydrophobic surfaces as shown in Supplementary Information). This result is fully consistent with previous simulation data by Ho et al. who reported that CO_2 adsorption in water confined in hydrophilic nanoporous silica pertains to a confinement-induced oversolubility effects (45).

We now investigate the impact of CO_2 solubility/adsorption on the line tension τ. Fig. 3(a) shows τ for water/CO_2 systems at different CO_2 partial pressures p_g. A significant dependence of τ on p_g is observed. More precisely, in the absence of CO_2, line tensions of -2.4 pN and -1.2 pN are measured for the hydrophobic and hydrophilic solids, respectively. Increasing

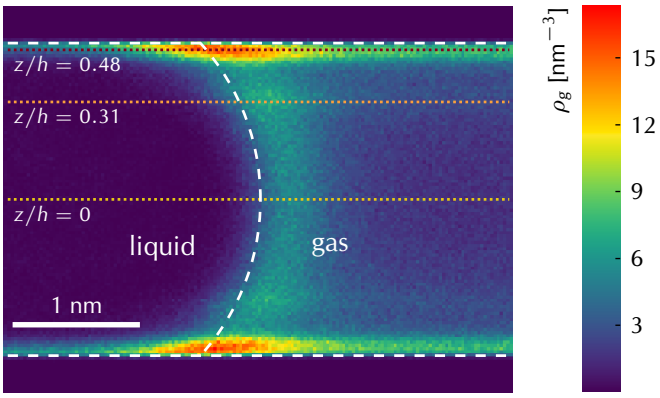

A

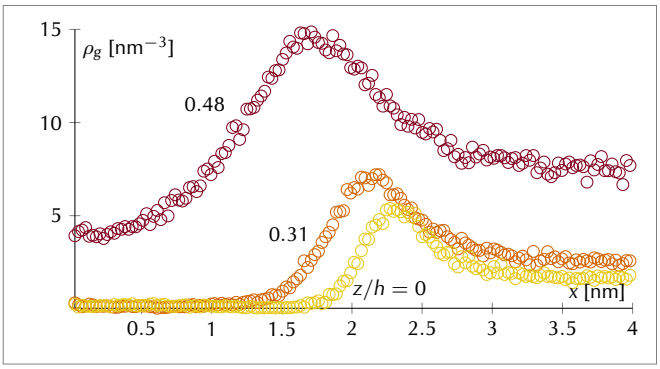

B

Fig. 2. A CO_2 density map in the case of a liquid water droplet within a hydrophobic confinement (*see text*) in equilibrium with a CO_2 gas phase at 4.3 MPa. CO_2 is preferentially adsorbed at interfaces and triple line. Gibbs interfaces, defined using a water zero-adsorption criterion, are indicated as white dashed lines. B Horizontal CO_2 concentration profile at three different heights.

p_g up to 4.3 MPa reduces monotonously the line tension to -7.3 pN and -16.9 pN for the hydrophobic and hydrophilic solids, respectively. This result indicates, especially for the hydrophilic solid, that the free energy of the triple line is very sensitive to its chemical composition. For the hydrophilic solid, the magnitude of the line tension varies by more than one decade on this pressure range. The lowest negative line tension, $\tau = -16.9$ pN at a CO_2 pressure of 4.3 MPa, is four times smaller than the lowest value obtained for pure water (regardless, the solid hydrophilicity as recently shown by Bey *et al.* (9)).

In the case of the triple line between three-dimensional phases studied here, our results reveal that combined CO_2 adsorption at solid surfaces and at the triple line is accompanied by water depletion at the line and a major decrease of the negative line tension (i.e. which becomes even more negative) and hence an increase of the line free energy contribution. This behavior contrasts with that of lineactants adsorbed at a line within a two-dimensional biochemical membrane, which tend to reduce the positive line tension and, hence, the line free energy contribution (in a similar manner to a surfactant at a fluid interface).

Line tension and excess quantities at a triple line

The transition from a two-dimensional to a three-dimensional situation is a major change when considering the thermodynamics of line tensions (33). In the two-dimensional case of a straight line within a fluid interface at equilibrium, the surface tension of the interface is the same on both sides of the line. As a result, the force exerted along the line direction is independent of the positioning of the line. In this situation, the impact of adsorption on line tension can be modeled using a one-dimensional Gibbs relation analogous to the two-dimensional Gibbs relation used to model interfaces; in practice, this corresponds to Eq. 1 without the second term of the right hand side. In the three-dimensional case, for a straight line at the intersection between three flat interfaces separating three fluid phases, the pressure within the three phases is uniform but the different surface tensions of these interfaces may differ from each other. These three surface tensions govern the three contact angles as described using the Neumann relation. As enlightened by Djikaev and Widom (40) following the work by Boruvka and Neumann (41), the expression of the force along the line direction has to remain independent of the convention used to position the interfaces (and, consequently, the line). This implies that the one-dimensional Gibbs relation, which characterizes the line tension, comprises an additional term related to the work associated to changes in contact angles between interfaces (40)

$$d\tau = -\sum_{i=1}^{n} \Lambda_i d\mu_i + \sum_{\alpha=1}^{3} C_\alpha d\theta_\alpha \qquad [1]$$

where the index i refers to the different species, n is the total number of species, here $n = 2$, Λ_i are line concentrations, μ_i are chemical potentials, the index α refers to the different phases, θ_α are contact angles between the different phases, and C_α are mechanical potential associated with the contact angles. Here, the line tension τ, which follows the definition by Djikaev and Widom (40), corresponds to the *tensile force* as defined by Boruvska et al (41). The last term in Eq. 1 is required to take into account changes in the excess energy associated to interactions between the three phases at the contact line (induced by contact angle variations). To our knowledge, the determination of C_α functions, which are known to depend on the convention chosen to position the contact line, is still an open question. With curved interfaces, i.e. when there is a pressure difference between the different phases, additional terms are presumably contributing (41). If the system comprises now a solid phase – a situation of interest from a practical viewpoint, the question of the validity of the Gibbs adsorption equation at the line has not been addressed yet. In such a situation, for a straight contact line as considered in this paper, simplifications may arise as the orientations of the two surfaces are imposed by the orientation of the solid surface. However, in return, one would have to take into account the fact that the solid cannot be described thermodynamically by an isotropic pressure (so that the line tension is not anymore an intrinsic parameter (42)). For instance, in Eq. 20, which is used to compute the line tension throughout this article, τ depends explicitly on the geometric parameters h and θ_Y (see Materials and Methods). In summary, for such a system, there is at this stage no available theoretical prediction for the dependence of the line tension on a change in chemical potential (in particular of a solute). As a practical attempt to rationalize the variation of the line tension for a standard position of the line, we compare it to the variation $d\tau_\Lambda$ defined as the first term of Eq. 1. This contribution is defined from the following Gibbs relation:

$$d\tau_\Lambda = -\Lambda_g d\mu_g - \Lambda_l d\mu_l \qquad [2]$$

with Λ_g and Λ_l the excess quantities at the triple line of the gaseous solute and solvent (with μ_g, μ_l their chemical potentials). None of these linear adsorption contributions can be neglected *a priori* as previously stated. In this article, the classical definition consisting in setting the solvent adsorption to zero at the solid/liquid and liquid/gas interfaces is adopted. Using a different interface definition would lead to different values for linear adsorption and line tension (42). However, with this particular definition, as detailed below, the integration of Eq. 2 leads to variations $\Delta\tau_\Lambda$ which correspond to the measured variations of τ (see Materials and Methods) with the partial pressure p_g. Uncertainties, unless explicitly shown with error bars, are of the order of the marker size in each graph.

From a numerical point of view, Eq. 2 cannot be used readily from forces and densities computed in molecular simulation as it depends on chemical potentials (that are not directly measurable). To obtain an explicit expression for $\Delta\tau_\Lambda(p_g)$ as a function of measurable parameters, we replace the chemical potentials in Eq. 2 using the Gibbs relations for the bulk liquid and gas phases, respectively:

$$\begin{aligned} d(p_l + p_o) &= \rho_l d\mu_l + \rho_o d\mu_g \\ d(p_v + p_g) &= \rho_v d\mu_l + \rho_g d\mu_g \end{aligned} \qquad [3]$$

with p_l the pressure of a pure solvent in liquid phase at a given chemical potential μ_l and p_o the osmotic pressure induced by the solubilized gas (43). p_g and p_v are the solute and solvent partial pressures in the gas phase, (ρ_o, ρ_l) and (ρ_g, ρ_v) the solute and solvent densities in the liquid and the gas phases. By neglecting the variation of ρ_l upon solute solubilization, we can separate the terms in the first line of Eq. 3 to obtain $dp_l = \rho_l d\mu_l$. Assuming that the gaseous phase is an ideal gas mixture, we can separate the solute and solvent components in the second line of Eq. 3: $dp_g = \rho_g d\mu_g$ and $dp_v = \rho_v d\mu_l$. Once injected in Eq. 2, these expressions lead to a new formula for the derivative τ_Λ with respect to the solute partial pressure p_g:

$$\frac{\partial \tau_\Lambda}{\partial p_g} = -\frac{\Lambda_g}{\rho_g} - \frac{\Lambda_l}{\rho_l}\frac{\partial p_l}{\partial p_g} \qquad [4]$$

Qualitatively, the first term on the right hand side, associated to a positive solute line concentration, contributes to a decrease of the line tension while the second term, associated to the negative solvent line concentration, leads to an increase of it. To get a quantitative evaluation of these two terms, we express the derivative $\partial p_l / \partial p_g$ according to measured parameters. The liquid and gas pressures are related to surface energies of wet and dry solid surfaces, γ_w and γ_d, through a force balance in the x direction:

$$h\,(p_l + p_o) - 2\gamma_w = h(p_g + p_v) - 2\gamma_d \qquad [5]$$

The variation of the surface energy of each solid surface type is given by the Gibbs adsorption equation:

$$d\gamma_i = -\Gamma_i d\mu_g \qquad [6]$$

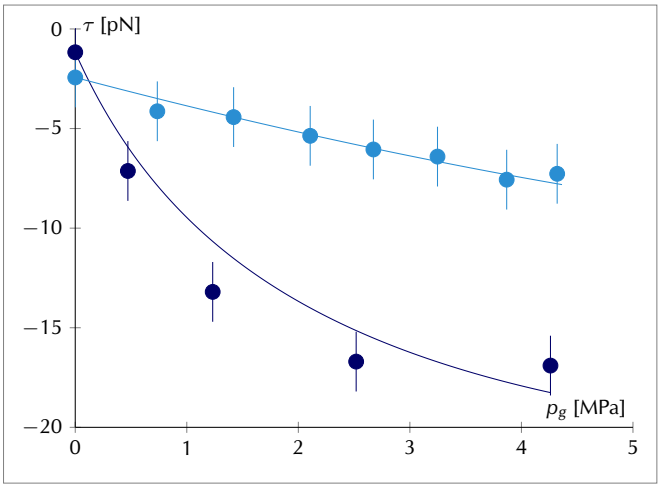

A

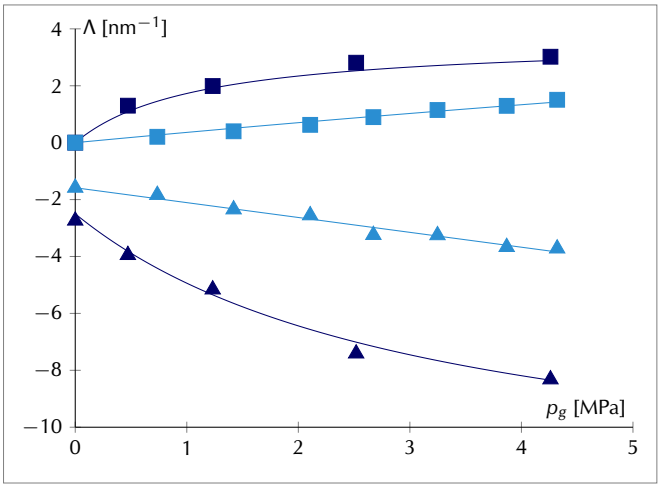

B

Fig. 3. Line tension τ A and linear excess Λ B of water (triangle) and CO_2 (square) as a function of the CO_2 partial pressure p_g in the case of a water liquid droplet confined between either hydrophilic (dark blue) or hydrophobic (light blue) surfaces. The symbols are numerical measurements while the lines are models based on a simple Langmuir adsorption law and Gibbs relation applied to line quantities.

with Γ_i the gas adsorbed amount on the wet solid (i=w) or on the dry solid (i=d). In Eq. 6, the solvent contribution has been neglected. With the solid surface position defined using the solvent zero-adsorption convention at the solid/liquid interface, the solvent surface concentration is zero at this interface and appears to be negligible at the solid/gas interface (see Materials and Methods). As a result,

$$d\gamma_w - d\gamma_d = (\Gamma_d - \Gamma_w)\, d\mu_g \qquad [7]$$

Let us denote $\Delta\Gamma = \Gamma_d - \Gamma_w$ the difference in surface adsorption at the wall/gas and wall/liquid interfaces.

Assuming Henry-type gas solubility and dilute ideal water/CO_2 mixtures, the osmotic pressure p_o with respect to the solute partial pressure in the gas phase p_g can be expressed using van't Hoff law, $p_o = Kp_g$, where $K = 0.19$ is the dimensionless Henry coefficient for CO_2 in water (see Materials and Methods). The partial derivative $\partial p_l/\partial p_g$ can be obtained from Eq 5 using Eq. 7 to express the derivative of $\gamma_w - \gamma_d$ and neglecting $\partial p_v/\partial p_g$ (as justified below) and the variation of h with p_g (as justified in Materials and Methods):

$$\frac{\partial p_l}{\partial p_g} = 1 - K + \frac{2}{h}\frac{\partial(\gamma_w - \gamma_d)}{\partial p_g} = 1 - K + 2\frac{\Delta\Gamma}{h\rho_g} \qquad [8]$$

The thermodynamical equilibrium of the solvent in the liquid phase at partial pressure p_l and in the vapor phase at partial pressure p_v leads to:

$$\frac{\partial \mu_l}{\partial p_g} = \frac{1}{\rho_l}\frac{\partial p_l}{\partial p_g} = \frac{1}{\rho_v}\frac{\partial p_v}{\partial p_g} \qquad [9]$$

As $\rho_v \ll \rho_l$ at the temperature and pressures considered here, Eq. 9 implies that $\partial p_v/\partial p_g$ is indeed negligible with respect to $\partial p_l/\partial p_g$ (which justifies our approximation to neglect this contribution in Eq. 8).

The prediction of $\Delta\tau_\Lambda$ as a function of p_g can be obtained by integrating Eq. 4 in which $\partial p_l/\partial p_g$ is replaced by Eq. 8. The water liquid density $\rho_l \simeq 33$ nm^{-3} is considered as constant (see Materials and Methods).

$$\Delta\tau_\Lambda(p_g) = -\int_0^{p_g}\left(\frac{\Lambda_g}{\rho_g} + \frac{\Lambda_l}{\rho_l}\left(1 - K + 2\frac{\Delta\Gamma}{h\rho_g}\right)\right)dp \qquad [10]$$

In this integral, four quantities – Λ_g, Λ_l, $\Delta\Gamma$ and ρ_g – depend on the gas pressure p_g. These line, surface and bulk densities are modeled using simple continuous functions fitted on discrete measurements of these densities as a function of p_g (see table 1). The relation between the CO_2 gas pressure p_g and density ρ_g is modeled using a second order virial expansion

$$p_g = k_B T \rho_g\,(1 - a\rho_g) \qquad [11]$$

with $a = 0.176$ nm^3. As shown in figure 4A, this expression is in agreement with available literature data (44). Following a phenomenological approach, both the surface and line concentration variations with respect to their value in the absence of gas are modeled with Langmuir type laws based on the solute pressure in the gas phase p_g

$$\Delta\Gamma(p_g) = \frac{k_\Delta\, p_g}{k_B T(1 + p_g/p_\Delta)} \qquad [12]$$

$$\Lambda_i(p_g) - \Lambda_{i0} = \frac{\kappa_i\, p_g}{k_B T(1 + p_g/p_{\Lambda_i})} \qquad [13]$$

where k_Δ and κ_i denote the surface and linear adsorption coefficient (in units of length and surface), p_Γ and p_{Λ_i} are characteristic saturation pressures. At low pressure, $\Delta\Gamma$ and Λ_i are of the order of $k_\Delta\rho_g$ and $\kappa_i\rho_g$. The index i refers either to the solvent l or the solute g. Fitting parameters are summarized in table 1. The difference $\Delta\Gamma(p_g)$ in CO_2 surface concentration at the solid/gas and solid/liquid interface is shown in the inset of Fig. 4A. These data reveal quantitatively the larger adsorption of CO_2 at the hydrophilic surface than at the hydrophobic one.

The dependence of p_l on p_g (used in Eq. 4 to express the solvent chemical potential as a function of p_g) is obtained from Eqs. 12 and 11 in Eq. 8. The fitting parameters in Eq. 12 are thus chosen to agree with the measured liquid pressures $p_l + p_o$ as expressed from the integral of Eq. 8

$$p_l + p_o - p_{l0} = p_g + \frac{2}{h}\int_0^{p_g}\frac{\Delta\Gamma}{\rho_g}dp \qquad [14]$$

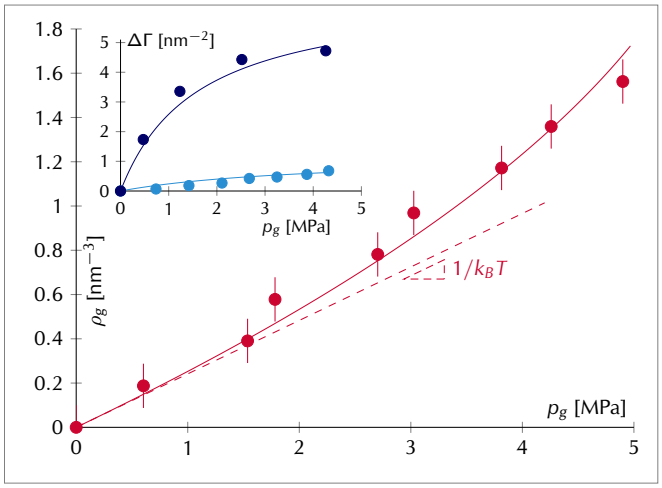

A

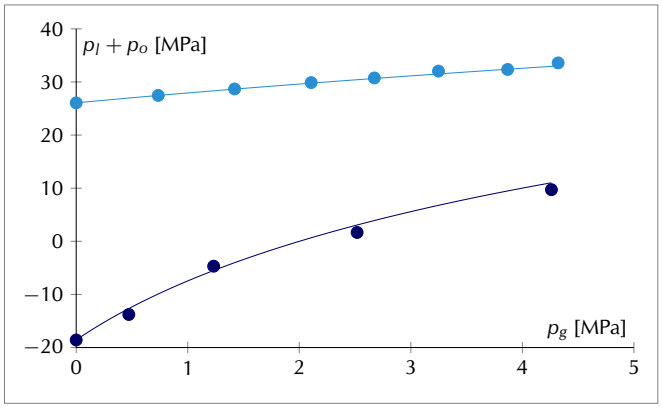

B

Fig. 4. A Dependence of the CO_2 density ρ_g in the gas phase on its partial pressure p_g. The red marks are simulated data while the continuous line is a second order virial decomposition. The dashed line is the ideal gas law. Inset: Difference between the CO_2 surface concentrations at the solid/gas and solid/liquid interfaces. B Dependence of the liquid pressure $p_l + p_o$ on the gas pressure p_g. Dark blue: hydrophilic solid, light blue: hydrophobic solid. The marks are simulated data while the lines are fitted against Langmuir adsorption law and Gibbs-Duhem relation (*see text*).

Integrals of Eq. 10 and Eq. 14 are easily evaluated from analytical expressions as detailed in the Materials and Methods section. As shown in Fig. 4B and inset of Fig 4A, the same set of parameters k_Δ and p_Δ leads to a good agreement with the simulated data for both $\Delta\Gamma$ and the liquid pressure (in particular for the hydrophilic solid where a significant variation of both quantities is observed). Due to the surface hydrophilicity, the liquid phase is under a negative pressure of the order of -20 MPa in the absence of CO_2. This pressure increases more rapidly than the pressure p_g and becomes positive for large p_g due to capillary effects related to CO_2 adsorption at the solid surfaces. This suggests that a Langmuir adsorption model is a reasonable approximation to describe these data. As shown in Fig. 3B, we observe that the line concentration Λ_g is positive and increases with p_g while the line concentration Λ_l is negative and decreases with p_g (therefore corresponding to a negative value for κ_l). As shown in Fig. 3B, a good agreement is observed between the simulated line concentrations and the fits using Eq. 13. This suggests that a Langmuir type law is still relevant to model line adsorption. At this stage, it becomes possible to compare the measured line tension τ with the value derived from the excess line concentrations $\tau_0 + \Delta\tau_\Lambda$ using Eq. 10 (see solid lines in Fig. 3A). For both the hydrophilic and hydrophobic solids, the two line tensions are in good agreement. This suggests that the angular terms introduced by Boruvka and Neumann (41) are of minor importance in our case owing to the use of the solvent zero-adsorption convention to position the interfaces. For the hydrophobic solid, the surface energies are weakly dependent on the gas solute pressure. As a result, the angles θ_α vary only little with pressure, which may explain why the last term of Eq. 1, in particular, is not contributing. For the hydrophilic surface, however, the situation is different as the contact angle increases significantly upon increasing the pressure. In this situation, the last term in Eq. 1 may contribute unless the C_α coefficients are small enough (which is suggested by our results). As $\rho_g/\rho_l \ll 1$ on the whole pressure range considered in our study, the magnitude of the negative first term is larger than the magnitude of the positive second term on the right hand side of Eqs. 4 and 10. As a result, a decrease of the line tension is observed. In other words, despite water molecule depletion at the triple line ($\Lambda_l < 0$), which is in magnitude larger than CO_2 accumulation at the triple line ($\Lambda_g > 0$), for both the hydrophilic and hydrophobic solids, our results suggest that the solute contribution Λ_g/ρ_g prevails over the solvent contribution $\Lambda_l/\rho_l \times \partial p_l/\partial p_g$. The derivative of the pressure p_l with respect to p_g in Eq. 10 is a smaller contribution $1 - K + 2\Delta\Gamma/(h\rho_g)$ than the ratio ρ_l/ρ_g. This means that the decrease in the line tension is mainly driven by the accumulation of CO_2 at the triple line. The CO_2 is thus acting as a line active agent which amplifies the thermodynamical contribution of the line – by up to an order of magnitude for the hydrophilic solid.

θ_Y	h [nm]	k_Δ [nm]	p_Δ [MPa]	κ_g [nm^2]	p_{Λ_g} [MPa]	κ_l [nm^2]	p_{Λ_l} [MPa]
64°	2.6	17	1.6	14	1.1	-13	3.2
126°	2.5	1.2	4	1.5	∞	-2.2	∞

Table 1. Fitting parameters for CO_2 adsorption at the solid surface (k_Δ, p_Δ), CO_2 adsorption at the triple line (κ_g, p_{Λ_g}), and water depletion at the triple line (κ_l, p_{Λ_l}) as a function of the CO_2 gas pressure p_g (see text). The indicated contact angles correspond to the data for pure water ($p_g = 0$ MPa).

Line active species and heterogeneous nucleation

In contrast to a triple line involving a single fluid (for which the line tension seems to be mainly driven by the contact angle (9)), fluid mixtures such as those studied here reveal various solute effects on the line tension. This complex behavior is expected to strongly impact heterogeneous nucleation of bubbles, droplets and even solids. Reversely, the large variability of experimental line tensions reported in the literature – in particular, those extracted form heterogeneous nucleation experiments – could be related to such specific solute and solvent effects at the triple line (6). In the framework of the classical nucleation theory (CNT), the nucleation rate of a stable nucleus is proportional to $\exp(-\Delta\Omega^*/(k_BT))$. The critical energy barrier $\Delta\Omega^*$ to be overcome to form such a stable nucleus comprises both bulk and surface contributions. However,

for a nucleus having a nanometric critical size, several works indicate that this theory fails to predict nucleation rates unless the line contribution is taken into account (5, 6, 11, 12). In this case, the critical energy barrier is complemented by an additional line tension term $\tau\mathcal{L}^*$ where $\mathcal{L}^*$ is the length of the triple line delimiting the critical nucleus. Considering the archetypical problem of heterogeneous nucleation of a spherical cap on a flat surface, the critical radius of curvature r^* of the cap is controlled by the difference in chemical potentials between the nucleus and the surrounding phase. While r^* is independent of the line tension, the circumference of the triple line $\mathcal{L}^* = 2\pi r^* \sin\theta^*$ depends on it (in the spirit of the critical contact angle θ^* which is by the modified Young equation $\cos\theta^* = \cos\theta_Y - \tau/(\gamma r^* \sin\theta^*)$ where θ_Y is the Young contact angle (46)). Typically, for a negative line tension, θ^* decreases as τ becomes even more negative. As a result, the volume of the critical cap corresponding to a fraction of the sphere of radius r^* becomes smaller with τ becoming even more negative (see inset in Fig 5A). In this configuration, taking into account through the modified Young equation the fact that half of the line energy contribution is balanced by a fraction of volume and surface terms, the energy barrier is (46)

$$\Delta\tilde{\Omega}^* = \Psi(\theta^*) + \tilde{\tau}\sin\theta^* \qquad [15]$$

where $\Delta\tilde{\Omega}^* = \Delta\Omega^*/(\pi\gamma r^{*2})$ is the dimensionless energy barrier and $\tilde{\tau} = \tau/(\gamma r^*)$ the dimensionless line tension (33). The positive dimensionless function $\Psi(\theta^*) = (2 - 3\cos\theta^* + \cos^3\theta^*)/3$ corresponds to the remaining fraction of volume and surface contributions. This function increase with θ^*. As θ^* depends on $\tilde{\tau}$, the line tension has a double effect on $\Delta\tilde{\Omega}^*$. As shown in Fig. 5A, for instance, a negative $\tilde{\tau}$ decreases $\Delta\tilde{\Omega}^*$ because of the second term in Eq. 15 but also, indirectly, because of the decrease of Ψ induced by a smaller contact angle $\theta^* < \theta_Y$ (see dashed line in Fig. 5A). For θ_Y in the range 60° to 120°, both contributions evolve almost linearly with $\tilde{\tau}$ while maintaining other physicochemical parameters constant.

In this study, the line tension is tuned through the solute gas pressure p_g. For the water/CO_2 mixture confined between hydrophobic surfaces, the solid surface properties are only slightly dependent on p_g with a minor relative change in $\cos\theta_Y$ as compared to the relative change in τ (see Fig. 3A and Materials and Methods). The dependence of the dimensionless energy barrier $\Delta\tilde{\Omega}^*$ with $\tilde{\tau}$ follows almost the light blue case in Fig. 5A with a range of $\tilde{\tau}$ depending on the radius of curvature r^* of the nucleus cap. This radius r^* reflects the supersaturation of the native binary mixture (8). The line tension τ itself might depend on the curvature of the triple line and, hence, on r^* (41). Nevertheless, as this dependence is quantitatively unknown, it is neglected here as a first order approximation.

The hydrophobic solid is however a particular case; in general, changing p_g is likely to impact line properties as well as surface properties. This illustrates the fact that changing specifically the properties of a triple line only is not trivial. For the water/CO_2 mixture confined between hydrophilic surfaces, we observe both an important change in τ and $\cos\theta_Y$. This reflects mainly the impact of CO_2 adsorption on the solid surfaces – especially on the solid/gas interface and, to a lower extent, on the liquid/gas surface tension γ. Surface adsorption reduces $\cos\theta_Y$ and, hence, $\Psi(\theta^*)$. As shown in Fig. 5B, for large r^*, the bulk and surface contributions dominate so that

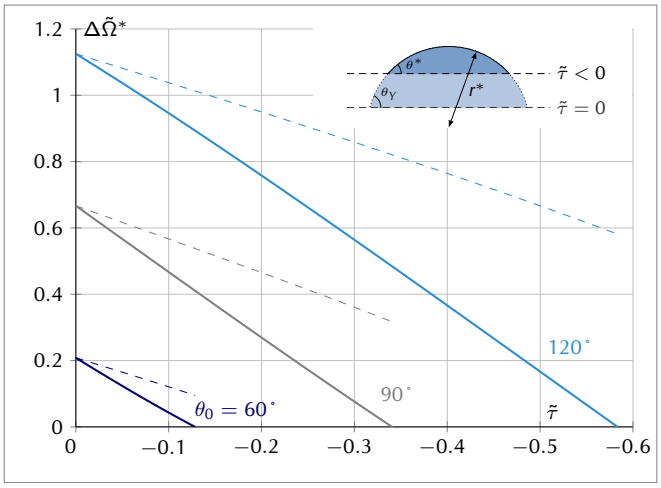

A

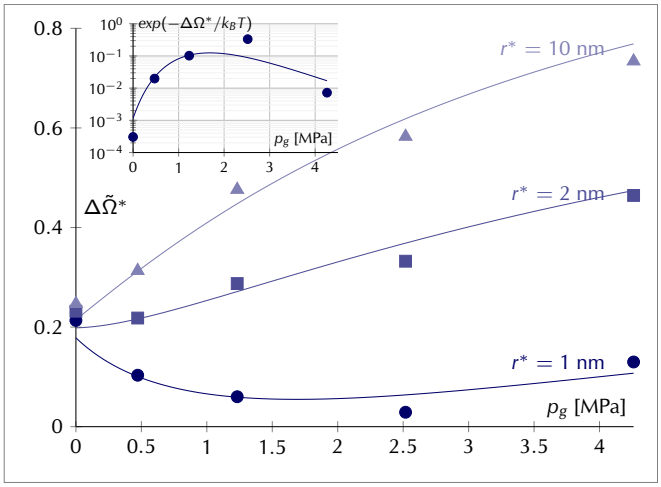

B

Fig. 5. A Dimensionless energy barrier $\Delta\tilde{\Omega}^*$ (full curve) according to the dimensionless line tension $\tilde{\tau}$ for a hemispherical cap on a flat surface (see inset). These data were determined by assuming a constant macroscopic contact angle θ_Y and critical radius r^* (see text). Sum of the bulk and surface contributions (dashed line) as a function of the change in the critical angle θ^* induced by the line tension (see text). B Dependence of $\Delta\tilde{\Omega}^*$ in the water/CO_2 mixture confined between the hydrophilic surfaces as a function of p_g. The symbols correspond to estimations based on measured values of τ, $\cos\theta_Y$ and γ. The lines correspond to the expressions of τ (Eq. 10, Fig. 3A) and $p_l + p_o$ (Eq. 14, Fig. 4B) as a function of p_g without any additional fitting parameters (see Materials and Methods).

one observes an increase in $\Delta\tilde{\Omega}^*$ (leading to hampered nucleation). For small r^*, however, the line contribution plays also a role and the decrease in the negative τ when increasing p_g tends to reduce Ψ. For $r^* = 1$ nm, one observes a competition between the line and the surface/bulk contribution which leads to a non monotonic evolution of $\Delta\tilde{\Omega}^*$ as p_g is varied. For p_g around 2 MPa, $\Delta\tilde{\Omega}^*$ reaches a minimum with a value that is an order of magnitude smaller than the one measured in the absence of CO_2. As shown in the inset of Fig 5B, this minimum corresponds at room temperature to an increase by three orders of magnitude of the nucleation rate with respect to its value in the absence of CO_2. Our results for r^* smaller than 1 nm suggest that negative $\Delta\tilde{\Omega}^*$ could be reached, therefore corresponding to spontaneous droplet nucleation. CO_2,

through its coupled action at the solid surface and triple line, can act either as a strong nucleation inhibitor or promotor. This important result indicates that the contribution of line active molecules at a triple line may be far from negligible. Specific trends may be observed according to the chemical component under consideration and its specific action on line tension. In addition, the morphology/topology of the solid surface where the nucleus grows is expected to impact the geometry of the nucleus and the triple line as well as it thermodynamical contribution to line tension. In particular, the case of seed particles (of interest for atmospheric phenomena) and nanopores (of interest for mixture stability in porous media) may deviate from the flat surface considered here (6, 11, 47). Finally, we considered here surface and line tension values at equilibrium. However, nucleation being an out of equilibrium process, adsorption kinetics at the triple line and interfaces may play a key role. Surface and line tensions as well as surface and line concentrations may evolve during nucleation.

Conclusion

We have shown that a gaseous solute may accumulate at a solid/liquid/gas triple line where it plays the role of a line active agent. To rationalize the impact of such solute accumulation, line excess concentrations have been introduced in a thermodynamically consistent manner. These excess concentrations depend on the convention used to position the line, which is itself related to the convention used to position the interfaces between the three phases in contact at the triple line. The use of the Gibbs convention of zero-adsorption for the solvent at the liquid/gas interface and at the solid/liquid interface allows defining unambiguously both the position of the solid/gas interface and triple line. With such a convention, even in the absence of gas solute, the solvent presents a non-zero excess concentration at the line (which turns out to be negative for water). Upon increasing the solute gas pressure, the solvent line concentration decreases while the solute line concentration increases. These two contributions impact the line tension due to the chemical potential variation for the solute and solvent induced upon increasing the solute gas pressure. Using this surface and line position convention, we have shown that the simple Gibbs law applied to line quantities is sufficient to give a reasonable prediction for the line tension. In particular, no additional angular terms – that were suggested in several theoretical works (40) – were needed to capture the change in the line tension; however, we acknowledge that these terms might be not negligible for other surface and line position conventions. To our knowledge, this is the first time that such measurements are sensitive enough to proceed reliably to such a comparison. It appears that solvent depletion at the line tends to increase the line tension while solute adsorption tends to decrease its value. However, for the CO_2 pressure range considered in our study, water depletion has a limited impact on line tension due to the limited variation in its chemical potential upon changing the CO_2 pressure. This leads to a monotonic decrease of the line tension for the hydrophilic and hydrophobic surfaces being mainly attributed to the CO_2 accumulation at the line. With hydrophilic surfaces, the negative line tension in the absence of CO_2 becomes even more negative – by more than an order of magnitude – when the CO_2 gas pressure reaches 3 MPa. This means that the negative free energy associated to the triple line, which becomes ten times larger, is expected to lead to an important decrease in the nucleation energy barrier (with a massive increase by several orders of magnitude in the nucleation rate). These results show that the line tension may be an important parameter in the modeling of the nucleation rate for binary mixtures when considering nanometric critical nuclei. This might be of importance either for nanometric seed aerosol in the atmosphere or for gas capture in highly confined environments (18). Our work provides important microscopic insights in adsorption effects at the triple line that is limited to perfectly smooth solid walls and equilibrium systems. Further work is needed to better understand the impact of solid structure and the kinetics of line adsorption.

Materials and Methods

Water/CO_2 mixtures. In the case of aqueous simulations we use SPC/E (48) (water) and EPM2 (49) (CO_2) molecular models, and the dispersive interactions of water atoms with CO_2 atoms are set according to Lorentz-Berthelot rules. These models have been calibrated to reproduce the properties of pure homogeneous phases and they under-estimate both CO_2 solubility in liquid water and CO_2 adsorption at liquid-gas interfaces (44, 50). The Henry constant relating the osmotic pressure $k_BT\rho_o$ to the gas pressure is $K = 0.19$ (see Fig. 6A) while the value measured with real water/CO_2 is 0.83 (51). Rigid molecular models miss variations of molecular polarization that play an important role in solubilization and adsorption (19, 50). Despite their limitations, these models are used in molecular simulations to provide a first insight in adsorption effects without relying on computationally demanding polarizable models, and the adsorption effects that are measured in this article are consequently probably lower bounds of real phenomena.
We consider slits that are formed by two dispersive walls, the interaction of which with each fluid atom is modeled by a 9-3 external potential:

$$u(z) = \varepsilon_w \left[\frac{2}{15} \left(\frac{\sigma_w}{z - z_w} \right)^9 - \left(\frac{\sigma_w}{z - z_w} \right)^3 \right] \qquad [16]$$

with σ_w the interaction range, ε_w the interaction strength, z the vertical coordinate of the interacting atom and $z_w \pm 1.45$ nm the positions of the walls. We consider successively two types of wall, one that is hydrophobic and one that is hydrophilic. The interaction of water oxygens with the walls are accounted for using $\varepsilon_w = 2.51$ kJ/mol and $\varepsilon_w = 6.27$ kJ/mol for hydrophobic and hydrophilic walls, respectively, and $\sigma_w = 3$ Å. The hydrogen atoms of water do not interact with the walls. Hydrophobic and hydrophilic walls feature contact angles of respectively $\theta = 126°$ and $\theta = 64°$ in the case of pure water simulations. The interaction of carbon and oxygen atoms of CO_2 molecules with the walls are induced using Lorentz-Berthelot rules (see Supplementary Information for details). A cutoff radius $r_c = 9$ Å is applied to dispersive inter-atomic interactions. Long range electrostatic interactions are computed using the PPPM algorithm (52) and the spurious electrostatic interactions between periodic images in the z direction are reduced using Yeh and Berkowitz's methodology (53) adding three empty boxes. We simulate $n_l = 1152$ water molecules in contact with $n_g = [0, 40, 80, 120, 160, 200, 240, 280]$ (hydrophobic) and $n_g = [0, 160, 320, 480, 640]$ (hydrophilic) CO_2 molecules. The box dimensions are $L_x = 12$ nm, $L_y = 4$ nm, $L_z = 3.75$ nm. The temperature $T = 300$ K is close to the critical temperature of CO_2 ($T_c = 304$ K), but the gas pressure remains lower than the critical pressure ($p_c = 7.4$MPa). SHAKE algorithm is used to constrain water molecules to a rigid geometry (54). The integration timestep is set to $\Delta t = 1$ fs, and the thermostat damping time to $t_T = 1$ ps. Each simulation is run for a total duration $t = 50$ ns, 5 ns of which are used to let the system relax, and 45 ns to record equilibrium properties. In both simulation series (hydrophilic or hydrophobic case), the liquid water density varies less than 0.5% and is considered as constant. Error bars ($\pm 1 s.d.$) are computed using the block averaging methodology (55) with blocks of size $t_b = 450$ ps.

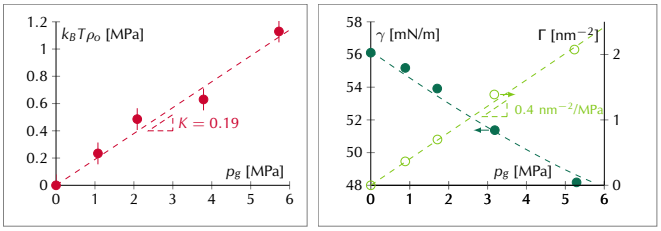

A B

Fig. 6. A Osmotic pressure calculated from solubilized CO_2 density ρ_o according to the CO_2 gas pressure p_g, numerical measurements (symbols) are linearly fitted (dashed line) to extract the Henry constant K. B Surface tension of a flat water/gas interface according to the CO_2 gas pressure p_g (left axis) and CO_2 concentration at the water/gas interface (right axis). Numerically measured concentration (open symbol) is linearly fitted (light green dashed line). Numerically measured surface tension (full symbol) is interpolated (dark green dashed line) from the integration of the interfacial Gibbs-Duhem relation without any additional free parameter (*see text*).

Surface tension measurements. For each simulation, the value of the liquid-gas surface tension γ is necessary to compute the line tension τ and the contact angle θ through Eqs. 20 and 22. Moreover, the adsorption of solute at the liquid-gas interface modifies the value of γ that therefore varies from one system to another. To measure the dependence of γ on the solute concentration Γ, we run additional simulations of planar liquid films in contact with gas phases of various compositions (see Fig. 6B). We use the classical mechanical methodology (56) to measure γ. The liquid film is formed by $n_l = 3456$ water molecules set in contact with $n_g = [0, 100, 200, 400, 800]$ CO_2 molecules in a periodic box of size $L_x = L_y = 4$ nm, $L_z = 30$ nm for a total duration $t = 50$ ns. The surface concentration, which follows a Henry's regime, increases linearly with the CO_2 gas pressure p_g with a slope $k_\Gamma = 0.403$ nm^{-2}/MPa (see Fig. 6B). The dependance of the surface tension γ on p_g is expressed integrating the Gibbs-Duhem relation

$$\gamma = \gamma_0 - \int_0^{p_g} \frac{\Gamma}{\rho_g} dp = \gamma_0 - k_\Gamma (k_B T)^2 \rho_g \left(1 - \frac{3}{2}a\rho + \frac{2}{3}a^2\rho_g^2\right) \quad [17]$$

where γ_0 is the surface tension measured with pure water, and ρ_g expressed according to p_g inverting the second order expansion Eq. 11

$$\rho_g = \frac{1}{2a}\left(1 - \sqrt{1 - \frac{4ap_g}{k_BT}}\right) \quad [18]$$

Line tension measurement. The measurement of line tensions τ in molecular simulations commonly rely either on the geometric study of spherical droplets (32) or on the thermodynamic integration of the free energy during the quasistatic filling of a pore (57). In this paper we use a third, mechanical methodology that has recently been published by the authors (9). This methodology avoids certain biases of the geometric methodology while being computationally cheaper than the thermodynamic integration methodology. The mechanical approach relies on the computation of the total forces Σ_x, Σ_y and Σ_z that are exerted by the fluid phase on the boundaries of the simulation box (see Fig. 1 and (9)). Σ_z is measured as the vertical force applied by the fluid phase on the lower wall, and Σ_x, Σ_y are measured using the virial equation as the force opposing the extension of box's lengths L_x and L_y, respectively (58, 59):

$$\Sigma_\alpha = \left\langle -\frac{(n_g + n_l)k_BT}{L_\alpha} + W_\alpha \right\rangle \quad [19]$$

with $\alpha = x, y$ the horizontal directions, W_α the energy derivative relative to a homogeneous affine expansion of the fluid coordinates in the direction α and $\langle ... \rangle$ the thermodynamic average. As derived in Bey *et al.* (9), the line tension τ can be measured by combining the forces Σ_x and Σ_y with the geometric parameters h, L_x, L_y and θ_Y, and the liquid-gas surface tension γ:

$$\tau = \frac{1}{4}(\Sigma_y - \Sigma_x \frac{L_x}{L_y}) - \gamma h \Phi(\theta_Y) \quad [20]$$

with $\Phi(\theta)$ a trigonometric function, that weakly depends on the contact angle θ_Y:

$$\Phi(\theta_Y) = \frac{1}{4}\left(\sin(\theta_Y) - \frac{\theta - \pi/2}{\cos(\theta_Y)}\right) \quad [21]$$

Moreover, expressing the vertical force Σ_z as a combination of fluid pressures and liquid-gas surface tension, a mechanical expression of the contact angle θ_Y is derived

$$\cos\theta_Y \simeq \frac{h}{l}\left[\frac{1}{2\gamma L_y}\left(\Sigma_z + (p_g + p_v)L_xL_y\right) - 1\right] \quad [22]$$

with p_g and p_v the partial pressures in the gas phase of solute and solvent, respectively, and l the distance between curved liquid/gas interfaces at the center of the pore (see Fig. 1 and (9)). As the triple line is straight in the simulated configurations, the line tension does not contributes to the contact angle which indeed corresponds to the Young contact angle for the considered pore size (see Fig. 7A and (9)). In our simulations we deduce p_g and p_v from the densities of solute and solvent in the gas phase. In the case of water/CO_2 mixtures, only a few water molecules are present in the gas phase and p_v is negligible. The relation between p_g and ρ_g is obtained running simulations of a pure phase of $n_g = [12, 25, 37, 50, 62, 75, 87, 100]$ CO_2 molecules confined in a periodic box of size $L_x = L_y = L_z = 4$ nm for a total duration $t = 5$ ns. In all the simulations, the distance l and the confinement h are computed applying the criterion of solvent zero-adsorption at liquid-gas and solid-liquid interfaces: $l = [n_- - \rho_v L_x]/[\rho_l - \rho_v]$ and $h = n_|/\rho_l$ with n_- and $n_|$ the average number of solvent molecules per unit of surface area in slabs located in the center of the pore that are perpendicular to the z and x directions, respectively. This definition of confinement leads to $h \sim 2.6$ nm which varies slightly with adsorption phenomena when changing p_g (see Fig. 7A). These confinements are large enough relatively to the 9-3 wall-fluid potential under consideration (Eq. 16) to avoid a variation of the equilibrium contact angle induced by disjoining pressure effects (see Supplementary Information).

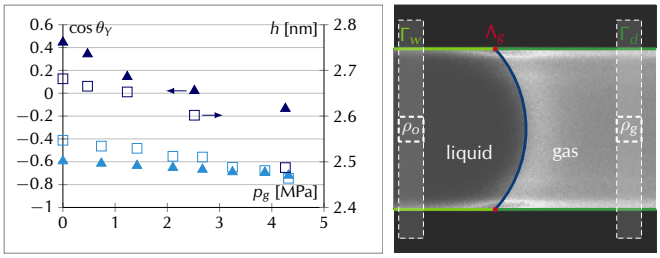

A B

Fig. 7. A Dependance of the contact angle (triangle, left axis) and height of the pore (square, right axis) on the gas pressure p_g for hydrophilic walls (dark blue) and hydrophobic wall (light blue). B Illustration of the measurement process of CO_2 surface concentration at solid/gas Γ_d and solid/liquid Γ_w interfaces as well as CO_2 line concentration Λ_g (see text).

Wall and line excess concentrations. Line excess concentrations are extracted from the total number of molecules minus the number of molecules in liquid and gas phases on the one hand, and molecules adsorbed at each interfaces on the other hand (see Fig. 7B). Concerning the liquid/vapor interface, its CO_2 content (per unit length in the y direction) is given by the product of the surface excess concentration Γ (known according to p_g from independent simulations of planar liquid films, see Fig. 6B) by the interface arc length $\mathcal{L}_i = |\beta|\, h/\cos\theta$ where $\beta = \theta - \pi/2$ stand for half the arc angle as detailed in (9),. The excess surface concentration in CO_2 at solid/liquid walls is extracted from the number of molecules contained within a vertical slab of fluid positioned at the center of the liquid region minus the number of molecules associated to bulk phases, while the excess surface concentrations in CO_2 and water at solid/vapor interfaces are obtained following the same procedure in the vapor region far from the liquid/gas interface (see Fig. 7B). The content in bulk phases is obtained multiplying the volume of each

slab by the molecular density measured within small boxes either in the liquid of gas phase at the center of the slit (see Fig. 7B). In the hydrophilic case, the CO_2 concentration at solid/liquid interface Γ_w is more than five time smaller than the concentration Γ_d at the solid/gas interface; a single Langmuir type model is used to approximate the difference $\Delta\Gamma = \Gamma_d - \Gamma_w$. In the hydrophobic case both surface concentrations increase almost linearly with p_g, with Γ_w being at most half of Γ_d. The water surface concentration at solid/gas interface is in both hydrophilic and hydrophobic case more than three orders of magnitude smaller than CO_2 surface concentration. Total surface content are deduced from surface concentrations multiplied by the area of the respective solid/liquid or solid/gas interface defined from the values of L_x, l, h and θ_Y. As detailed in (9), the distance between the two contact lines on one wall (see Fig. 1) is $w = l - 2h(1-\cos\beta)/\sin\beta$ and the section of liquid (in the zx plane) is $A_L = hw + h^2(\beta - \cos\beta\sin\beta)/(4\sin^2\beta)$. Consequently, the CO_2 line concentration is

$$\Lambda_g = n_g/L_y - 2\mathcal{L}_i\Gamma - 2\left(\Gamma_d L_x - \Delta\Gamma w\right) - \left(hL_x\rho_g - A_L(\rho_{g-}\rho_o)\right) \quad [23]$$

The water line concentration Λ_l is obtained in the same manner with respective water density and water surface concentrations.

Analytical expressions of line tension and pressure variations. To calculate the integrals in Eq. 10 and Eq. 14, partial fraction decomposition of Eq. 12 and Eq. 13 is required. For this purpose we define $\varrho_\alpha = p_\alpha/(k_BT)$ where α is either Δ, Λ_l or Λ_g and we introduce the densities ρ_α^+ and ρ_α^- defined as:

$$\rho_\alpha^\pm = \frac{1}{2a}\left(1 \pm \sqrt{1+4a\varrho_\alpha}\right) \quad [24]$$

We define also functions $f_\alpha(\rho_g)$ and $g_\alpha(\rho_g)$ of the form

$$f_\alpha(\rho_g) = \frac{\rho_\alpha^+ + 2\varrho_\alpha}{\rho_\alpha^+ - \rho_\alpha^-}\ln\left(\frac{\rho_\alpha^- - \rho_g}{\rho_\alpha^-}\right) - \frac{\rho_\alpha^- + 2\varrho_\alpha}{\rho_\alpha^+ - \rho_\alpha^-}\ln\left(\frac{\rho_\alpha^+ - \rho_g}{\rho_\alpha^+}\right) \quad [25]$$

$$g_\alpha(\rho_g) = \frac{\varrho_\alpha}{a\rho_l(\rho_\alpha^+ - \rho_\alpha^-)}\ln\left(\frac{\rho_\alpha^-(\rho_\alpha^+ - \rho_g)}{\rho_\alpha^+(\rho_\alpha^- - \rho_g)}\right) + \frac{2\varrho_\alpha}{\rho_\alpha^+ - \rho_\alpha^-}\left(\frac{\rho_\alpha^-}{\rho_l}\ln\left(\frac{\rho_\alpha^- - \rho_g}{\rho_\alpha^-}\right) - \frac{\rho_\alpha^+}{\rho_l}\ln\left(\frac{\rho_\alpha^+ - \rho_g}{\rho_\alpha^+}\right)\right) \quad [26]$$

After some algebra, neglecting h variations with p_g, Eq. 14 writes

$$p_l + p_o - p_{l0} = p_g + 2p_\Delta\left(f_\Delta(\rho_g) - 2a\rho_g\right)\frac{k_\Delta}{h} \quad [27]$$

and Eq. 10 writes

$$\Delta\tau_\Lambda = -\kappa_g p_{\Lambda_g}\left(f_{\Lambda_g}(\rho_g) - 2a\rho_g\right) - 2\Lambda_{l0}\frac{p_\Delta}{\rho_l}\left(f_\Delta(\rho_g) - 2a\rho_g\right)\frac{k_\Delta}{h} - (1-K)\left(\left(\kappa_l p_{\Lambda_l} + \Lambda_{l0}k_BT\right)\frac{\rho_g}{\rho_l}(1 - a\rho_g) + \kappa_l p_{\Lambda_l} g_{\Lambda_l}(\rho_g)\right) - 2\kappa_l p_{\Lambda_l}\frac{k_\Delta\varrho_\Delta}{h\rho_l}\left(\frac{p_\Delta f_\Delta(\rho_g)}{p_\Delta - p_{\Lambda_l}} + \frac{p_{\Lambda_l} f_{\Lambda_l}(\rho_g)}{p_{\Lambda_l} - p_\Delta} - 2a\rho_g\right) \quad [28]$$

where ρ_g expresses according to p_g using Eq. 18.

Nucleation energy barrier. The contact angle θ^* according to the line tension is obtained from a numerical minimum search to respect the modified Young equation for a given value of θ_Y. To fit the dependence of the energy barrier $\Delta\tilde{\Omega}^*$ according to p_g considering simultaneous surface tension and line tension changes, the Young contact angle dependance on p_g is expressed with $\cos\theta_Y = h(p_l + p_o - p_g)/(2\gamma)$ using Eq. 27 for the liquid pressure dependance on p_g and considering for simplicity a constant values $h = 2.6$ nm and $\gamma = 0.05$ N/m.

ACKNOWLEDGMENTS. This work was supported by the French Research Agency (ANR TAMTAM 15-CE08-0008 and LyStEn 15-CE06-0006). We thank E. Charlaix for fruitful discussions and NVIDIA Corporation for the donation of a Tesla K40 GPU used for this research. We acknowledge as well the Centre Informatique National de l'Enseignement Supérieur (CINES) for a generous supercomputer allocation (project: A0040807695).

1. Muller P, Galet F (1991) First Measurement of the liquid-solid line energy in a langmuir monolayer. *Physical Review Letters* 67(9):1106–1110.
2. Blanchette CD, Lin Wc, Orme CA, Ratto TV, Longo ML (2007) Using Nucleation Rates to Determine the Interfacial Line Tension of Symmetric and Asymmetric Lipid Bilayer Domains. *Langmuir* 23:5875–5877.
3. Bischof AA, Mangiarotti A, Wilke N (2015) Soft Matter. *Soft Matter* 11:2147–2156.
4. Rowlinson JS, Widom B (1982) *Molecular Theory of Capillarity*. (Dover Publications, Mineola, Etats-Unis).
5. Gretz RD (1966) The line-tension effect in heterogeneous nucleation. *Surface Science* 5:239–251.
6. Hienola AI, et al. (2007) Estimation of line tension and contact angle from heterogeneous nucleation experimental data. *Journal of Chemical Physics* 126(094705).
7. Kikby J, et al. (2011) Role of sulphuric acid, ammonia and galactic cosmic rays in atmospheric aerosol nucleation. *Nature* 476:429–435.
8. Wyslouzil BE, Wölk J (2016) Overview : Homogeneous nucleation from the vapor phase — The experimental science. *Journal of Chemical Physics* 145(211702):1–26.
9. Bey R, Coasne B, Picard C (2020) Probing the concept of line tension down to the nanoscale. *Journal of Chemical Physics* 152(094707).
10. Zhao B, et al. (2019) Resolving the Apparent Line Tension of Sessile Droplets and Understanding its Sign Change at a Critical Wetting Angle. *Physical Review Letters* 123(94501):1–6.
11. Guillemot L, Biben T, Galarneau A, Vigier G, Charlaix E (2012) Activated drying in hydrophobic nanopores and the line tension of water. *Proc. Natl. Acad. Sci. U.S.A.* 109(48):19557–19562.
12. Tinti A, Giacomello A, Grosu Y, Casciola CM (2017) Intrusion and extrusion of water in hydrophobic nanopores. *Proc. Natl. Acad. Sci. USA* 114(48):E10266–E10273.
13. Winter D, Virnau P, Binder K (2009) Monte Carlo Test of the Classical Theory for Heterogeneous Nucleation Barriers. *Phys. Rev. Lett.* 103(22).
14. Singh H (2016) A critical review of water uptake by shales. *Journal of Natural Gas Science and Engineering* 34:751–766.
15. Ho LN, Clauzier S, Schuurman Y, Farrusseng D, Coasne B (2013) Gas Uptake in Solvents Confined in Mesopores: Adsorption versus Enhanced Solubility. *J. Phys. Chem. Lett.* 4(2013):2274.
16. Clauzier S, Ho LN, Pera-Titus M, Coasne B, Farrusseng D (2012) Enhanced H2 Uptake in Solvents Confined in Mesoporous Metal- Organic Framework. *J. Am. Chem. Soc.* 134(2012):17369.
17. Coasne B, Farrusseng D (2019) Gas Oversolubility in Nanoconfined Liquids: Review and Perspectives for Adsorbent Design. *Microp. Mesop. Mater.* 288(2019):109561.
18. Iglauer S (2017) CO_2 –Water–Rock Wettability: Variability, Influencing Factors, and Implications for CO_2 Geostorage. *Acc. Chem. Res.* 50(5):1134–1142.
19. Hamm LM, Bourg IC, Wallace AF, Rotenberg B (2013) Molecular Simulation of CO_2- and CO_3-Brine-Mineral Systems. *Rev. Mineral. Geochem.* 77(1):189–228.
20. Bagherzadeh SA, Englezos P, Alavi S, Ripmeester JA (2012) Influence of Hydrated Silica Surfaces on Interfacial Water in the Presence of Clathrate Hydrate Forming Gases. *J. Phys. Chem. C* 116(47):24907–24915.
21. Liang Y, Tsuji S, Jia J, Tsuji T, Matsuoka T (2017) Modeling CO_2 –Water–Mineral Wettability and Mineralization for Carbon Geosequestration. *Acc. Chem. Res.* 50(7):1530–1540.
22. Veluswamy HP, et al. (2016) Rapid methane hydrate formation to develop a cost effective large scale energy storage system. *Chemical Engineering Journal* 290:161–173.
23. Pefoute E, Prager M, Russina M, Desmedt A (2016) Quasi-elastic neutron scattering investigation of the guest molecule dynamics in the bromomethane clathrate hydrate. *Fluid Phase Equilibria* 413:116–122.
24. Jin D, Coasne B (2017) Molecular Simulation of the Phase Diagram of Methane Hydrate : Free Energy Calculations , Direct Coexistence Method, and Hyperparallel Tempering. *Langmuir* 33:11217–11230.
25. Maheshwari S, Kruijsdijk CV, Sanyal S, Harvey AD (2020) Nucleation and Growth of a Nanobubble on Rough Surfaces. *Langmuir* 36:4108–41015.
26. Angulo A, [van der Linde] P, Gardeniers H, Modestino M, Rivas] DF (2020) Influence of bubbles on the energy conversion efficiency of electrochemical reactors. *Joule* 4(3):555 – 579.
27. Broom DP, et al. (2016) Outlook and challenges for hydrogen storage in nanoporous materials. *Applied Physics A* 122(151):1–21.
28. Camisasca G, Tinti A, Giacomello A (2020) Gas-Induced Drying of Nanopores. *The Journal of Physical Chemistry Letters* 11:9171–9177.
29. Amirfazli A, Neumann A (2004) Status of the three-phase line tension: a review. *Adv. Colloid Interface Sci.* 110(3):121–141.
30. Drelich J (1996) The significance and magnitude of the line tension in three-phase (solid-liquid-fluid) systems. *Colloids Surf., A* 116(1-2):43–54.
31. Sedlmeier F, et al. (2008) Water at polar and nonpolar solid walls (Review). *Biointerphases* 3(3):FC23–FC39.
32. Weijs JH, Marchand A, Andreotti B, Lohse D, Snoeijer JH (2011) Origin of line tension for a Lennard-Jones nanodroplet. *Phys. Fluids* 23(2):022001.
33. Law BM, et al. (2017) Line tension and its influence on droplets and particles at surfaces. *Prog. Surf. Sci.* 92(1):1–39.
34. Petsev ND, Leal LG, Shell MS (2020) Universal gas adsorption mechanism for flat nanobubble morphologies. *Phys. Rev. Lett.* 125(14):146101.
35. Zhang XH, et al. (2004) Degassing and Temperature Effects on the Formation of Nanobubbles at the Mica/Water Interface. *Langmuir* 20(9):3813–3815.
36. Zhang XH, Maeda N, Hu J (2008) Thermodynamic Stability of Interfacial Gaseous States. *J. Phys. Chem. B* 112(44):13671–13675.
37. Powell MR, Cleary L, Davenport M, Shea KJ, Siwy ZS (2011) Electric-field-induced wetting

and dewetting in single hydrophobic nanopores. *Nat. Nanotechnol.* 6(12):798–802.
38. Leung K, Luzar A, Bratko D (2003) Dynamics of Capillary Drying in Water. *Phys. Rev. Lett.* 90(6).
39. Brown WM, Wang P, Plimpton SJ, Tharrington AN (2011) Implementing molecular dynamics on hybrid high performance computers – short range forces. *Comput. Phys. Commun.* 182(4):898–911.
40. Djikaev Y, Widom B (2004) Geometric view of the thermodynamics of adsorption at a line of three-phase contact. *J. Chem. Phys.* 121(12):5602–5610.
41. Boruvka L, Neumann AW (1977) Generalization of the classical theory of capillarity. *J. Chem. Phys.* 66(12):5464–5476.
42. Schimmele L, Napiórkowski M, Dietrich S (2007) Conceptual aspects of line tensions. *J. Chem. Phys.* 127(16):164715.
43. Fair JC, Oesterle JF (1971) Reverse Electrodialysis in Charged Capillary Membranes. *J. Chem. Phys.* 54(1971):3307.
44. Zhang H, Singer SJ (2011) Analysis of the subcritical carbon dioxide water interface. *J. Phys. Chem. A* 115(23):6285–6296.
45. Ho LN, Schuurman Y, Farrusseng D, Coasne B (2015) Solubility of Gases in Water Confined in Nanoporous Materials: ZSM-5, MCM-41, and MIL-100. *J. Phys. Chem. C* 119(2015):21547–21554.
46. Navascues G, Tarazona P (1981) Line tension effects in heterogeneous nucleation theory. *Journal of Chemical Physics* 75(5):2441–2446.
47. Iwamatsu M (2016) Line tension and morphology of a droplet and a bubble attached to the inner wall of a spherical cavity. *Journal of Chemical Physics* 144(144704):1–13.
48. Berendsen HJC, Grigera JR, Straatsma TP (1987) The missing term in effective pair potentials. *J. Phys. Chem.* 91(24):6269–6271.
49. Harris JG, Yung KH (1995) Carbon Dioxide's Liquid-Vapor Coexistence Curve And Critical Properties as Predicted by a Simple Molecular Model. *J. Phys. Chem.* 99(31):12021–12024.
50. Vlcek L, Chialvo AA, Cole DR (2011) Optimized Unlike-Pair Interactions for Water–Carbon Dioxide Mixtures Described by the SPC/E and EPM2 Models. *J. Phys. Chem. B* 115(27):8775–8784.
51. Diamond LW, Akinfiev NN (2003) Solubility of CO_2 in water from -1.5 to 100°C and from 0.1 to 100 MPa : evaluation of literature data and thermodynamic modelling. *Fluid Phase Equilibira* 208:265–290.
52. Hockney RW, Eastwood JW (1988) *Computer Simulation Using Particles*. (Adam Hilger, NY, Etats-Unis).
53. Yeh IC, Berkowitz ML (1999) Ewald summation for systems with slab geometry. *J. Chem. Phys.* 111(7):3155–3162.
54. Andersen HC (1983) Rattle: A "velocity" version of the shake algorithm for molecular dynamics calculations. *J. Comput. Phys.* 52(1):24–34.
55. Allen M, Tildesley DJ (1990) *Computer Simulation of Liquids*. (Oxford University Press, New York, Etats-Unis).
56. Kirkwood JG, Buff FP (1949) The Statistical Mechanical Theory of Surface Tension. *J. Chem. Phys.* 17(3):338–343.
57. Binder K, Block B, Das SK, Virnau P, Winter D (2011) Monte Carlo Methods for Estimating Interfacial Free Energies and Line Tensions. *J Stat Phys* 144(3):690–729.
58. Schofield P, Henderson JR (1982) Statistical Mechanics of Inhomogeneous Fluids. *Proc. R. Soc. A* 379(1776):231–246.
59. Thompson AP, Plimpton SJ, Mattson W (2009) General formulation of pressure and stress tensor for arbitrary many-body interaction potentials under periodic boundary conditions. *J. Chem. Phys.* 131(15):154107.